Selective tuning of order parameters of multiferroic $BiFeO_3$ in picoseconds using midinfrared terahertz laser pulses

Nan Feng,[1,*] Jian Han,[2,*] Chuwen Lan,[1,3] Ben Xu,[4,†] Ke Bi,[1,3,‡] Yuanhua Lin,[2] and Cewen Nan[2]

[1]*State Key Laboratory of Information Photonics and Optical Communications, School of Science, Beijing University of Posts and Telecommunications, Beijing 100876, China*

[2]*State Key Laboratory of New Ceramics and Fine Processing, School of Materials Science and Engineering, Tsinghua University, Beijing 100084, China*

[3]*Bejing University of Posts and Telecommunications Research Institute, Shenzhen 518057, China*

[4]*Graduate School, China Academy of Engineering Physics, Beijing 100193, China*

(Received 5 September 2021; accepted 7 December 2021; published 11 January 2022)

Selectively tuning the properties of a material with multiple order parameters, such as polarization and magnetization, requires precise control of the crystal structure. Recently developed midinfrared THz laser techniques provide an efficient way to manipulate the structure of materials at an ultrafast rate. This paper presents a methodology to evaluate the possibility of picosecond multiple switching of order parameters in perovskite structure oxides using first-principles calculations. With multiferroic $BiFeO_3$ as a model system, we demonstrate that the desired property can be tuned by an external laser pulse's perturbation with frequency 15.2 THz. The dynamics of phonon modes are illustrated, revealing that lasers enable switching of polarization and magnetization within 1 ps. The switching mechanisms can be attributed to the nonlinear coupling of the pumped infrared-active mode with the ferroelectric and antiferrodistortive modes. Our work provides an initiative for more detailed experimental investigations to explore light control orders and dynamic material design.

DOI: 10.1103/PhysRevB.105.024304

I. INTRODUCTION

Strongly correlated oxides exhibit a wide variety of functional properties with coupled electric, magnetic, and structural degrees of freedom that are now being developed for use in multiple state memory devices [1,2]. Perovskite structure oxide material ABO_3 provides a wide range of structural distortions with lattice instabilities of high-symmetry $Pm\bar{3}m$ structure [3,4]. For example, structural distortions, such as off-centering displacements of the A and B cations or a concerted rotation of the oxygen octahedra, result in a switchable ferroelectric polarization or magnetization [3]. Manipulation of their properties through the coupling between properties, order parameters, and crystal structures is extremely significant for applications.

However, the usual duration of the tuning process via strain, electric, or magnetic fields is limited above hundreds of picoseconds [5,6]. Therefore, a rising interest is vested in developing a technique to control and modify the order parameters of these materials within pico- or femtoseconds, aiming to accelerate the related applications on ultrafast memory devices. The availability of intense THz laser pulses provides an efficient way to meet this challenge, which has been demonstrated experimentally [7–9] and theoretically [10–12]. In particular, previous studies have demonstrated that the THz laser pulses in the midinfrared spectral range can coherently excite the phonon modes associated with the order parameters indirectly by externally pumping an infrared (IR) -active phonon mode at a higher frequency, to modulate the equilibrium of the structure into a transient state of modified orders [13]. It has also been used to drive switching of ferroelectric order in $PbTiO_3$ and $LiNbO_3$ [14,15], inducing ferroelectricity in strained $KTaO_3$ and $SrTiO_3$ [16,17], enhancement of superconductivity in $YBa_2Cu_3O_{6.5}$ [18,19], insulator-metal transitions in $Pr_{1-x}Ca_xMn\ O_3$ and $NdNiO_3$ [20–23], orbital order transition in $La_{0.5}Sr_{1.5}MnO_3$ [24,25], modulation of magnetic order in $NdNiO_3$ and Cr_2O_3 [26,27], excitation of a magnon in $ErFeO_3$ [28,29], and ferromagnetism in $DyFeO_3$ and $LaTiO_3$ [30,31]. Of the perovskites identified, the room-temperature multiferroic $BiFeO_3$ (BFO) [32] is highly tunable because the ferroelectric and antiferromagnetic vectors lock to each other, exhibiting the coexistence of multiple order parameters accompanied by different types of structural distortions. There is thus a strong incentive to put forth the idea using a midinfrared laser to modulate ferroelectricity and magnetization selectively. Recently, many efforts have been devoted to dynamic manipulation of the phonons and magnons in BFO [33–35]. The electric-field-driven ultrafast switching of polarization and magnetic chirality vector has been theoretically predicted in bulk BFO [36]. The ultrafast polarization dynamics over a 1 ps timescale upon excitation of ultrafast band-gap laser pulses has been shown in BFO thin film [37]. The photostriction effect generated by THz pulsed excitation has been found experimentally and theoretically [38,39]. Based on the photovoltaic effects, the fully optical control of the ferroelectric polarization has been observed in the BFO-based heterostructure [40]. The phase transition from the rhombohedral to tetragonal phase and ferroelectric domain structures

*These authors contributed equally to this work
†bxu@gscaep.ac.cn
‡bike@bupt.edu.cn

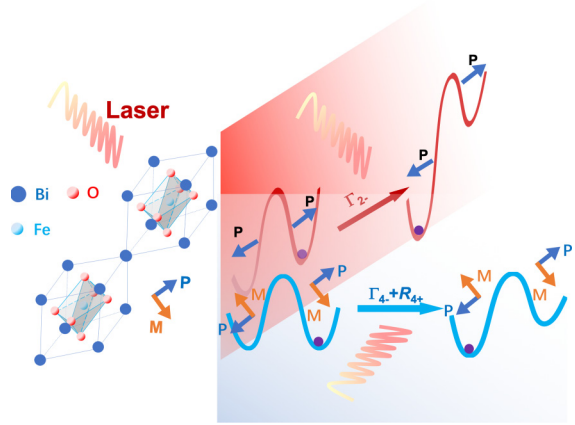

FIG. 1. Schematic for selective transition paths for polarization (red curve) and magnetization (dark blue curve) switching in $BiFeO_3$ under the illumination of a pulsed laser. The blue and orange arrows denote polarization and magnetization vectors, respectively. The dark purple balls correspond to the position of the potential energy minimum before and after laser illumination. The crystal distortions introduced by the laser illumination are labeled along the transition curves.

in mixed-phase BFO thin films have been experimentally modulated on a nanosecond timescale using extremely short laser pulses [41,42].

This work presents a scheme to realize the ultrafast switching of double option states with polarization or magnetization in perovskite structure oxides, i.e., multiferroic BFO in this study, by illuminating with a midinfrared laser pulse (shown in Fig. 1). In our case, comprehending the double-well shape of the energy surface as a function of amplitudes of the crystal distortions is the main motivation. The two stable minima correspond to the ground-state structures with opposite directions of polarization or magnetization. At equilibrium, the system is present in one of the two minima. During the transition, the system follows the transition path of structural distortions and achieves the transition of polarization and magnetization. The structural distortions will correspond to normal modes of the two ground-state structures, and that with the most substantial associated property will be selected. These modes can be large-amplitude coherently excited by a pumped higher-frequency IR lattice vibration mode through nonlinear coupling. Therefore, the strongest coupled IR mode needs to be identified, and the dynamic evolutions of these coupled phonons in response to the external perturbations should be discussed. This approach is introduced in detail in Sec. II. Our calculations reveal that the reversal of polarization and magnetization in BFO can occur within 1 ps, despite a relatively high external excitation. The switching mechanisms can be attributed to the nonlinear coupling of the pumped IR mode with the ferroelectric and antiferrodistortive modes. These methods and results could facilitate the dynamic material design and development of ultrahigh-speed memory storage devices.

II. METHODOLOGY

A. Obtaining distortion modes that are sensitive to property

Physical properties with different orders, polarization, and magnetization, for example, are dependent upon the corresponding structural modifications in perovskite materials (e.g., $SrTiO_3$, $PbTiO_3$, $BiFeO_3$, $LiNbO_3$). The local atomic distortion is one of the critical aspects in understanding structure-property relationships. These properties related to the distortion of crystals can be decomposed into several eigendistortion modes, which resemble natural Raman- or IR-active modes of crystals. Therefore, we are able to use these phonon modes to modify the structure order by coherently displacing the lattice along the phonon coordinates of the order parameter. The direct excitation of the modes of interest only limits us to IR-active modes. This limitation can be lifted by means of nonlinear coupling, in which these modes can be indirectly excited by a high-frequency IR mode. A sufficiently strong resonant excitation of these modes can significantly affect the macroscopic properties of materials on the picosecond timescale due to the changes in the bond angles and lengths [13]. Therefore, it is vital to obtain phonon modes that are most relevant to the desired physical properties. In particular, it is practical to proceed from the initial- and final-state configurations with the desired physical property changes, and to explore the possible phase-transition pathways between the two different order states using the nudged elastic band (NEB) method [43]. Subsequently, distortion modes with different origins and amplitudes are obtained by symmetrical analysis using programs such as ISODISTORT [44], thus decomposing the structural deviation of the end-point structures from the highest energy (saddle) point structure. To probe the microscopic mechanism of phase transition further, a set of structures are obtained through a linear interpolation of the atomic positions, while keeping the value of the amplitudes of these distortion modes constant. The fractional evolution of the structures along the path varies from -100% to 100%. Due to the second-order property of these phase transitions, a symmetric double-well potential energy profile is obtained for a different order. Note that some of the desired distortion phonon modes of the saddle structure will appear at the Γ point in the Brillouin zone of the initial/final-state structure [3,45] due to folding of the Brillouin zone for the distorted structures with a bigger unit cell.

The atomic displacements along the eigenvectors of a phonon mode for a set $\{\mathbf{q}, j\}$ with an amplitude $Q_{\mathbf{q}j}$ are given by $u_k = \frac{Q_{\mathbf{q}j}}{\sqrt{m_k}} W^k_{\mathbf{q}j}$ [20], where $\mathbf{q}$ is the wave vector, j is the band index, u_k is the displacement of the kth atom in Cartesian coordinates, and m_k is the atomic mass of this atom. $W^k_{\mathbf{q}j}$ is the corresponding eigenvector of the dynamical matrix $D(\mathbf{q})$ [46], given by

$$\sum_{k'\beta} D^{kk'}_{\alpha\beta}(\mathbf{q}) W^{\beta k'}_{\mathbf{q}j} = \omega^2_{\mathbf{q}j} W^{\alpha k}_{\mathbf{q}j}. \tag{1}$$

The corresponding eigenvalue $\omega_{\mathbf{q}j}$ provides the mode frequency, and the elements of the dynamical matrix are [46]

$$D^{kk'}_{\alpha\beta}(\mathbf{q}) = \sum_{l'} \frac{\Phi_{\alpha\beta}(0k, l'k')}{\sqrt{m_k m_{k'}}} e^{i\mathbf{q}\cdot[\mathbf{r}(l'k')-\mathbf{r}(0k)]}, \tag{2}$$

where $\alpha\beta$ are the Cartesian indices, $\Phi_{\alpha\beta}$ are the second-order force constants, and $\mathbf{r}(lk)$ is the equilibrium position of the kth

atom in the lth unit cell. $W_{\mathbf{q}j}$ is normalized and dimensionless, and mode amplitudes are given in $\text{Å}\sqrt{\text{amu}}$. Therefore, the eigenvector of every distortion mode can be obtained based on the displacements of all atoms in each transition structure.

Subsequently, it is necessary to obtain the possible resonant phonon modes which demonstrate similarities with the property-sensitive distortion modes. The phonon frequencies and eigenvectors in the initial-state phase are obtained using the frozen-phonon method as implemented in PHONOPY [46]. The similarity S overlaps between the normalized eigenvectors of the distortion modes $W^k(d)$, and the normal modes $W^k(j)$ of the initial structure are defined as their dot product [31],

$$S(j,d) = \left| \sum_k W^k(j) \cdot W^k(d) \right|, \tag{3}$$

where k is the atom index, and j is the index number of the one-phonon mode. Thus, the normal mode that most resembles the distortion mode is identified.

B. Introducing relative IR mode

Only IR-active phonons, which possess an electric-dipole moment, are directly excited by coupling to the electric field component of a laser pulse to yield large vibrational amplitudes [11,12]. Therefore, one crucial aspect of manipulating the order states is discovering the IR phonon modes that are responsible for the nonlinear coupling interactions. In most previous studies, the total energies as a function of all mode coordinates are fit with a polynomial to extract the nonlinear coupling coefficients [19]. Here, we consider these coupling coefficients to be physically the same as the scattering coefficients in phonon transport theory. Therefore, we first obtained the third-order force constants using the SHENGBTE software [47], which is frequently used in phonon transport analysis, and we extracted several potential IR modes that interacted with the distortion mode from their interaction strength using the PHONO3PY software [48].

The phonon-phonon interaction strength $\phi_{\mathbf{q}j,\mathbf{q}'j',\mathbf{q}''j''}$ among the three phonons $\{\mathbf{q}, j\}$ involved in the scattering is calculated from second- and third-order force constants, which can be expressed as [48]

$$\phi_{\mathbf{q}j,\mathbf{q}'j',\mathbf{q}''j''} = \frac{1}{\sqrt{N}} \frac{1}{3!} \sum_{kk'k''} \sum_{\alpha\beta\gamma} W_{\mathbf{q}j}^{\alpha k} W_{\mathbf{q}'j'}^{\beta k'} W_{\mathbf{q}''j''}^{\gamma k''} \sqrt{\frac{\hbar^3}{8 m_k m_{k'} m_{k''} \omega_{\mathbf{q}j} \omega_{\mathbf{q}'j'} \omega_{\mathbf{q}''j''}}}$$
$$\times \sum_{l'l''} \Phi_{\alpha\beta\gamma}(0k, l'k', l''k'') e^{i\mathbf{q}'\cdot[\mathbf{r}(l'k') - \mathbf{r}(0k)]} e^{i\mathbf{q}''\cdot[\mathbf{r}(l''k'') - \mathbf{r}(0k)]} e^{i(\mathbf{q}+\mathbf{q}'+\mathbf{q}'')\cdot\mathbf{r}(0k)} \delta(\mathbf{q}+\mathbf{q}'+\mathbf{q}''), \tag{4}$$

where $\delta = 1\,(=0)$ if $\mathbf{q}+\mathbf{q}'+\mathbf{q}''$ is (is not) a reciprocal-lattice vector. $\Phi_{\alpha\beta\gamma}$ denote the cubic force constants. N is the number of unit cells, $\hbar$ is the reduced Planck constant, and $\omega_{\mathbf{q}j}$ is the harmonic frequency.

C. Obtaining the energy surface

As discussed above, the displacements along the normal modes can be generated to modulate the structure. After obtaining the desired distortion and IR phonon modes, it is essential to express the amplitudes of the two-phonon mode dependence of the Hamiltonian of the system. Therefore, we carried out a series of calculations with different modulations of the amplitude of the distortion and IR modes. The X- and Y-axis correspond to the modulation of the distortion modes and the system's energy. Different branches of curves are obtained for various IR modulations. Since every structure is a superposition of displacements caused by all relevant distortion modes, we consider that all distortion modes are combined in the form of a full mode. Its amplitudes are computed for normalized eigenvectors obtained from the above displacement-amplitude function. We calculated the energy surface of the system $E(Q_{\text{IR}}, Q_{\text{P}})$ around the equilibrium position with the perturbation of IR and distortion modes. In this notation, Q_{IR} is the driving IR-mode amplitude, while Q_{P} corresponds to the full distortion-mode amplitude. Simulations in related works revealed that the $E(Q_{\text{IR}}, Q_{\text{P}})$ function is expanded to third-order in the centrosymmetric crystals, and the contributions of higher-order interaction terms are included in noncentrosymmetric crystals [13]. By performing the least-mean-square fitting of the above energy surface $E(Q_{\text{IR}}, Q_{\text{P}})$ using polynomials, the coupling coefficients are obtained. It should be noted that different behaviors are demonstrated for different classifications of phonons. The appearance of the asymmetric double-well potential energy surface is favorable, indicating that the corresponding IR mode is likely to represent the pumped mode that drives the order state transition.

D. Solving the equation of motion

Based on the above perturbated energy surface of the system, the equation of motion can be obtained by the first derivative of energy with respect to the modulation of each phonon branch. The number of equations depends on the types of variable of the phonon branches. Thus, the corresponding evolutions of the nonlinearly coupled IR and distortion modes are obtained by solving the equation of motion numerically. Unlike the distortion modes, the IR mode is pumped externally under a forcing term of the form $F(t) = F\sin(\omega t)e^{-t^2/(2\tau^2)}$, where F, τ, and ω are the amplitude, width, and frequency of the laser pulse [14]. In this manner, we investigated the light-induced dynamics by considering the distortion and IR modes as two coupled classical oscillators under a pumped pulse at time $t = 0$. Solving the damped second-order differential equation with initial conditions, for a given finite pump amplitude F, the Q_{IR} is driven to oscillation around its equilibrium position, and the distortion mode oscillates about a displaced position. Therefore, it can

be observed whether the averaged Q_P displacement has an opposite sign with respect to the initial condition. The behavior represents a change of the crystal structure and, as such, a change in the order parameter of the material.

E. Computational details on BFO

Density functional calculations were performed as implemented in the Vienna Ab Initio Simulation Package (VASP) based on the projector augmented wave (PAW) method [49–51]. The Perdew-Burke-Ernzerhof of spin-polarized generalized gradient approximation was employed [52]. PAW pseudopotentials with Bi($5d^{10}6s^26p^3$), Fe($3p^63d^64s^2$), and $O(2s^22p^4)$ valence electrons were used. All calculations were performed using an effective on-site Coulomb interaction with $U_{\text{eff}} = 4$ eV for the localized Fe d orbitals. The Brillouin zone was sampled on a $9 \times 9 \times 9$ k-point mesh grid. The plane-wave cutoff energy was set to 500 eV, and the energy convergence was 10^{-5} eV. The $2 \times 2 \times 2$ supercells and a $3 \times 3 \times 3$ k-point mesh were used for the calculations of the second-and third-order force constants. For the NEB calculation, the force was converged to less than 0.02 eV/Å. The polarizations of initial- and final-state configurations were calculated using the modern theory of polarization [53], and the $R\bar{3}c$ symmetry was used as the centrosymmetric reference structure [54]. Noncollinear self-consistent calculations were performed by taking spin-orbit coupling effects [55] into account to determine the easy axis for the energetically favorable spontaneous magnetization. The energy convergence criterion was increased to 10^{-8} eV to ensure accurate calculations of the energy differences between different magnetization directions on the order of meV.

III. RESULTS AND DISCUSSION

In this section, we report on the polarization and magnetization switching behaviors of perovskite BFO, which has been identified as a room-temperature multiferroic and which crystallizes in the rhombohedral $R3c$ structure. The ground-state structure can be visualized as an elongation of the ideal cubic perovskite structure ($Pm\bar{3}m$) along the [111] direction with the movement of cations relative to the anions along the [111] direction as well as the antiphase rotations of the adjacent FeO_6 octahedra around the cubic [111] axis [56]. It is observed that it exhibits the (111) plane as an easy magnetization plane and has no in-plane magnetization direction, consistent with previous reports [57]. Following the procedures in Sec. II A, we managed to detect the essential distortion modes associated with the switching of polarization **P** and magnetization **M**. Considering $R3c$ structures with polarizations of opposite signs as initial- and final-state configurations, we carried out NEB calculations and found two transition paths. The initial, saddle point, and final-state configurations for the two cases are shown in Fig. 2. The difference between these two paths is whether the oxygen octahedral rotations are switched or not in final-state configurations. Reversing the octahedral rotations will cause the reversal of the Dzyaloshinskii-Moriya vector, and subsequently **M** will reverse [58]. Therefore, these two pathways correspond to transitions with polarization switching only and the transition of both polarization and

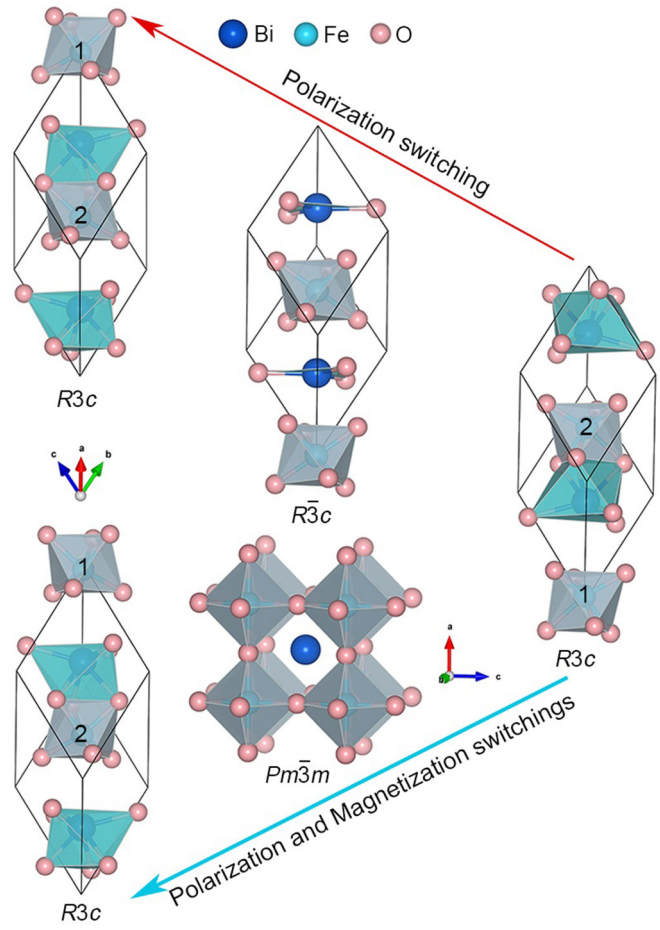

FIG. 2. Configurations of the ferroelectric switching pathways in $BiFeO_3$ with and without the reversal of the net magnetization for the initial state (right panel), saddle point (middle panel), and final state (left panel). FeO_6 and BiO_6 octahedra are shown in gray and light green, respectively. Two FeO_6 octahedra at different sites are shown with numbers for clarity.

magnetization. These two pathways of polarization switching for BFO are the same as the ones found by Munro *et al.* [59]. In the first case, the polarization direction changes from the [1,1,1] toward the $[\bar{1}, \bar{1}, \bar{1}]$ direction of the pseudocubic unit cell of BFO, while the net magnetization persists along the $[1, 1, \bar{2}]$ direction and does not reverse sign. The second path is the transition in the form of $\mathbf{P}[1, 1, 1] + \mathbf{M}[1, 1, \bar{2}] \rightarrow \mathbf{P}[\bar{1}, \bar{1}, \bar{1}] + \mathbf{M}[\bar{1}, \bar{1}, 2]$, i.e., switching magnetization in the presence of polarization switching. For convenience, we name the former case "PR" and the latter case "PMR" in the following discussion. The saddle point structures along the two paths possess the paraelectric-antiferromagnetic $R\bar{3}c$ and paraelectric-paramagnetic $Pm\bar{3}m$ symmetry, respectively, and they are both possible high-temperature paraelectric phases [54]. Therefore, it is essential to decompose the distortion modes of the two transition states.

The eigendistortion with a specifically permitted wave vector and an irreducible representation and the mode amplitude were obtained, comparing the parent saddle point structures with the $R3c$ structures of the end points. The main distortion modes for the two cases are illustrated in Fig. 3. First, for

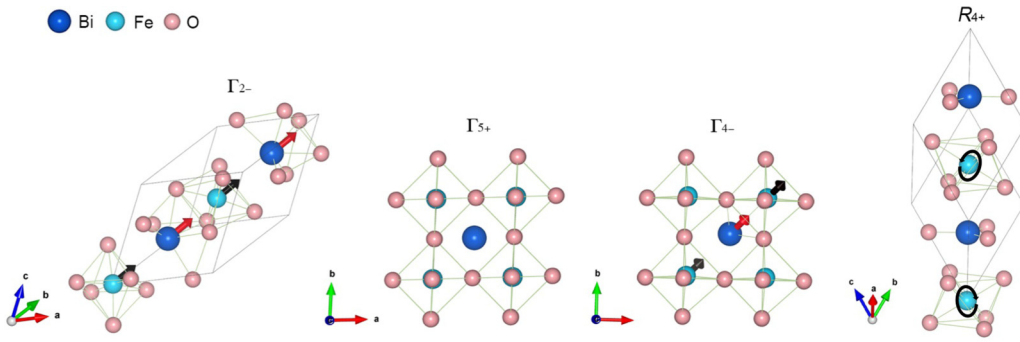

FIG. 3. Schematic of the most important distortion modes of the $R\bar{3}c$, and cubic $BiFeO_3$ structures with arbitrary amplitude, labeled with the irreducible representation of their unit cells.

the case with only polarization switching, the lattice deviates from the paraelectric $R\bar{3}c$ structure mainly in the following way, namely the ferroelectric-type distortions (labeled Γ_{2-}), the strain, and the oxygen octahedral rotations distortions (labeled Γ_{1+}). The Γ_{2-} involves the displacement of Bi and Fe atoms along the pseudocubic [111] direction. The strain mode describes the isotropic lattice expansion or contraction. The amplitude of the oxygen octahedral rotations of Γ_{1+} is negligible relative to that of R_{4+}, and the data are not demonstrated. On the other hand, the $R3c$ structure is the result of irrep distortions of the ideal cubic $Pm\bar{3}m$ structure associated with four different irrep modes: Γ_{1+}, Γ_{5+}, Γ_{4-}, and R_{4+}. The Γ_{5+} mode is related to a shear strain of the lattice. The zone center Γ_{4-} mode, which allows off-center ionic shifts along the pseudocubic [111] direction, contributes mainly to the spontaneous ferroelectric polarization. The zone boundary R_{4+} mode corresponds to an antiphase rotation of the FeO_6 octahedra around the pseudocubic [111] direction. These distortion mode driven ferroelectric and antiferrodistortive phase transitions are termed the FE and AFD modes. These distortion modes change their sign during the transition from initial to final state through saddle points, while the strain modes Γ_{1+} and Γ_{5+} only vary in amplitude.

To detect possible IR modes, the normal modes from the primitive magnetic unit cell of the initial state configuration were analyzed, comprising ten atoms, giving rise to 27 zone-center optical phonon modes with the decomposition $4A_1 + 5A_2 + 9E$. In these modes, A_1 and doubly degenerate E modes, which correspond to the dipole moments pointing along the z and in the x-y plane, respectively, are both Raman- and IR-active. In contrast, the A_2 modes are silent. The calculated zone-center phonon frequencies and their symmetries are given in Table I. The wave vectors of the $Pm\bar{3}m$ Brillouin zone are folded onto the smaller Brillouin zone of the low symmetric $R3c$ structure following the lattice reconstruction from these distortion modes. Therefore, the FE and AFD distortion modes will appear at the Γ point of the folded Brillouin zone, similar to what is observed for the perovskite oxide $PbZrO_3$ [3]. We identified the similarity of the modes (see Sec. II A) and found that the $A_1(9)$ [$A_1(12)$] mode eigenvector exhibits the most substantial overlap of 0.42 (0.49) with the FE (AFD) mode, i.e., $A_1(9)$ [$A_1(12)$] corresponds to the FE (AFD) distortion mode, consistent with previous calculations [60,61]. Therefore, it is reasonable to pump the IR modes of the $R3c$ phase to study the switching behaviors and their coupling strength.

Pumped by IR modes, distortion modes in the system will respond to these excitations with different strengths. To evaluate the phonon-phonon interaction strength and determine which IR mode can couple firmly to the distortion mode, we calculated the anharmonic coupling constants following Sec. II B, and we were primarily interested in the quadratic-linear coupling. According to the theory of ionic Raman scattering, the more significant the frequency difference between the driven Raman mode and the pumped IR mode is, the larger is the amplitude of the driven Raman mode [10,31,62]. The computed results between several highest-frequency IR modes and the $A_1(9)/A_1(12)$ modes are given in Table II. We detect the double-degenerate modes with an identical coupling strength, and the $E(22)$, $E(24)$, $E(27)$, and $A_1(29)$ IR modes with a coupling strength of 10^{-9}–10^{-8} eV. We note that the $A_1(29)$ mode strongly couples to the FE $A_1(9)$ and AFD $A_1(12)$ modes. The $A_1(9)$ also couples to $E(22)$, $E(24)$, and $E(27)$, but the coupling strength is around one order of

TABLE I. Calculated phonon eigenfrequencies in THz and their irreducible representation and optical activity of $R3c$ $BiFeO_3$. The mode index is given in the parentheses.

Irrep	Frequency (THz)	Optical activity
$A_1(9)$	4.67 (FE)	IR+Raman
$A_1(12)$	7.39 (AFD)	IR+Raman
$A_1(18)$	8.69	IR+Raman
$A_1(29)$	15.21 (IR)	IR+Raman
$A_2(6)$	3.09	Silent
$A_2(15)$	7.94	Silent
$A_2(19)$	9.45	Silent
$A_2(26)$	13.23	Silent
$A_2(30)$	18.25	Silent
$E(4,5)$	2.10	IR+Raman
$E(7,8)$	3.85	IR+Raman
$E(10,11)$	6.84	IR+Raman
$E(13,14)$	7.81	IR+Raman
$E(16,17)$	8.12	IR+Raman
$E(20,21)$	9.84	IR+Raman
$E(22,23)$	10.87	IR+Raman
$E(24,25)$	12.17	IR+Raman
$E(27,28)$	14.40	IR+Raman

TABLE II. For selected IR modes, the phonon-phonon coupling strength (10^{-9} eV) for the FE and AFD mode is listed. The mode index is given in the parentheses.

	FE	AFD
IR	$A_1(9)$	$A_1(12)$
$A_1(9)$	6.77	1.33
$E(22)$	1.28	1.92
$E(23)$	1.28	1.92
$E(24)$	5.04	75.16
$E(25)$	5.04	75.16
$E(27)$	1.43	22.62
$E(28)$	1.43	22.62
$A_1(29)$	14.4	58.19

magnitude smaller than the coupling to the $A_1(29)$ mode. We also notice that the coupling strength between the $A_1(29)$ and $A_1(12)$ modes is of the same order of magnitude (in fact, slightly larger) as that of the coupling to the $A_1(9)$ mode. The coupling strength of $E(24)$ with the $A_1(12)$ mode is the most dominant and strongest, closely followed by the $A_1(29)$ and $E(27)$ modes; in contrast, the interaction associated with the $A_1(9)$ mode is smaller.

Meanwhile, the effect of the IR modes is demonstrated in Fig. 4, where the potential energy profiles for PR and PMR with varying amplitudes of $E(22)$, $E(24)$, $E(27)$, and $A_1(29)$ are shown from panels (a) to (d), respectively. With the chosen IR modes (Fig. 4, top row), we compared the potential energy profiles following Sec. II C for the structures by combining the amplitudes of the IR modes and the full distortion modes associated with PR and PMR, obtained from the previous investigation with more detail from centrosymmetric positions (0% distortion) to the nonequilibrium noncentrosymmetric positions (−150% and 150% distortion), shown in Fig. 4, middle and bottom rows, respectively. Hereafter, the amplitudes of the full distortion modes are referred to as Q_{P} in order to be consistent with the definition introduced above, and the amplitudes of the IR-active modes Q_{IR} are referred to as Q_E or Q_{A1} according to their irreducible representations. In the absence of the IR mode, we found that the potential profile manifested a double-well shape exhibiting two stable minima, corresponding to the $R3c$ structure with opposite directions of polarization or magnetization. The $E(Q_{\mathrm{IR}}, Q_{\mathrm{P}})$ indicates the phase transition barrier calculated for $Pm\bar{3}m \rightarrow R3c$, which is 1.91 eV, and it is higher than the $R\bar{3}c$ to $R3c$ transition of 0.53 eV, which points to more difficulty in reversing the magnetization. For both cases, under a given value of the E-mode amplitude, the energy minimum of the distortion modes is displaced towards the opposite well and independent on the sign of Q_{IR}, which is required to drive the polarization and magnetization transition due to the breaking of the threefold rotational symmetry. The slight asymmetry of the IR mode

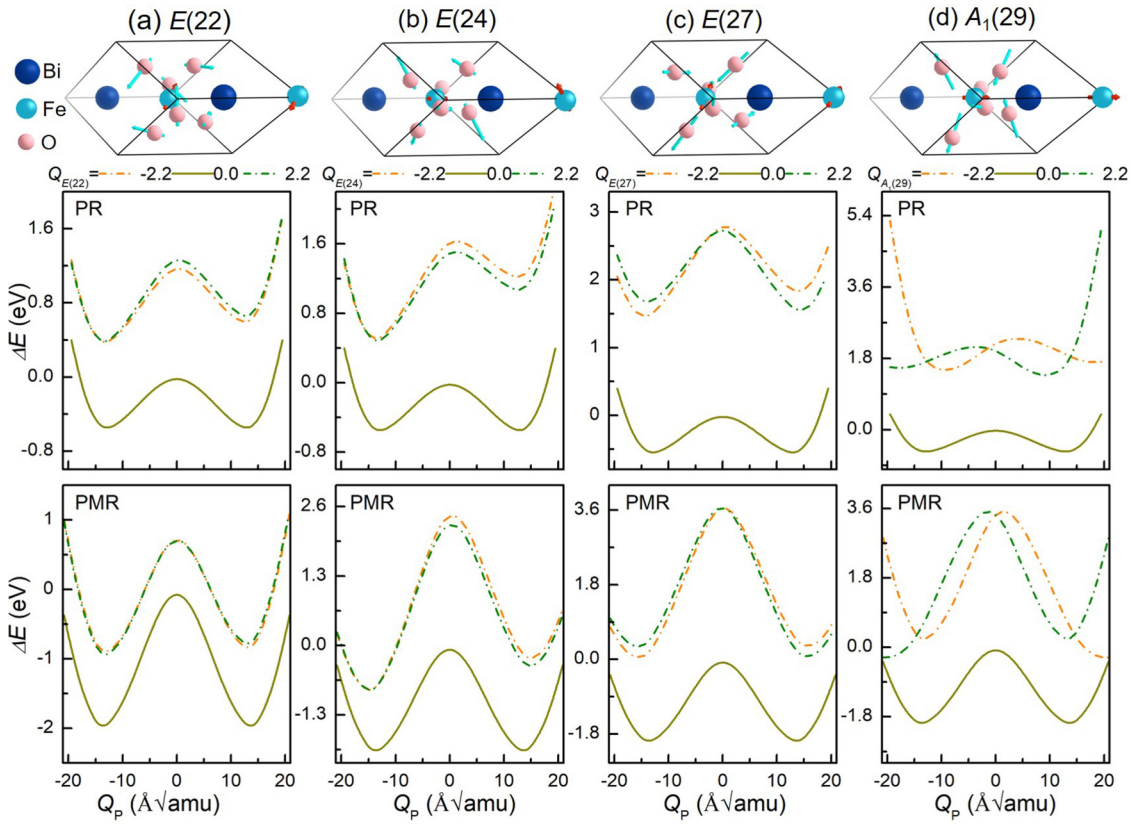

FIG. 4. (a)–(d) Comparison of the energy profiles for $E(22)$, $E(24)$, $E(27)$, and $A_1(29)$ mode amplitudes. (Top row) The corresponding atomic displacement patterns of IR-active modes associated with energy profiles for the nonlinear coupling of IR-active modes with the distortion modes for (middle row) polarization reversal (PR) as well as (bottom row) for polarization and magnetization reversal (PMR). We plot $\Delta E = E(Q_{\mathrm{IR}}, Q_{\mathrm{P}}) - E(0, 0)$ for visual purposes.

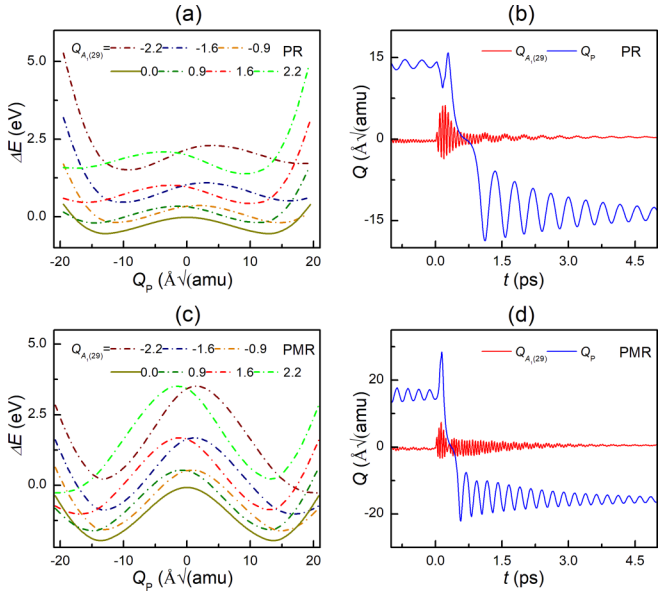

FIG. 5. Calculated total energy as a function of the distortion mode amplitudes for several values of the $A_1(29)$ mode amplitudes and the time evolutions for PR (a),(b) and PRM (c),(d). We plot $\Delta E = E(Q_{\rm IR}, Q_{\rm P}) - E(0,0)$ for visual purposes.

may originate from that the distortion mode of the X-axis, which is not identical to the corresponding mode of $R3c$ as described above. The energy surface is asymmetric for the $A_1(29)$ mode and will be discussed in detail later. In the case of PR (Fig. 4, middle row), we find that all of the considered E modes have a similar coupling strength to the $A_1(9)$ mode, one order of magnitude smaller than that of the $A_1(29)$ mode (see Table II), resulting in the energy difference between two double-wells of 0.27, 0.44, 0.37, and 0.22 eV for E (22), $E(24)$, $E(27)$, and $A_1(29)$, respectively, whereas the depth of the wells relative to the centrosymmetric reference structure obtained for them is 0.62, 0.58, 0.98, and 0.56 eV. For PMR (Fig. 4, bottom row), a smaller energy difference of the wells appears in the case of the $E(22)$ mode, although the depth of the wells is shallower than at origin, under the weakest coupling strength. The energy difference of the wells is largest (0.66 eV) for $E(24)$ and smallest (0.28 eV) for $E(27)$, with $A_1(29)$ intermediate (0.47 eV), and the depth of the wells increases least (0.89 eV) for the $E(24)$ mode, followed by (1.15 eV) for $A_1(29)$ and (1.48 eV) for the $E(27)$ mode, in line with the coupling strength results with the AFD mode, in competition with the FE mode.

As stated above, the interaction of the $A_1(29)$ mode with distortion modes is intensive. Therefore, we only consider the coupled dynamics of the $A_1(29)$ and distortion modes here. We extracted all possible nonlinear coupling terms following Sec. II C by fitting the comprehensive energy surfaces shown in Fig. 5 with the following polynomial expression, which is expanded up to fourth-order:

$$\begin{aligned} E(Q_{\rm IR},\ Q_{\rm P}) = {} & \tfrac{1}{2}\omega_{\rm IR}^2 Q_{\rm IR}^2 - \tfrac{1}{4}\omega_{\rm P}^2 Q_{\rm P}^2 + \tfrac{1}{3}a_3 Q_{\rm P}^3 + \tfrac{1}{4}a_4 Q_{\rm P}^4 \\ & + \tfrac{1}{3}b_3 Q_{\rm IR}^3 + \tfrac{1}{4}b_4 Q_{\rm IR}^4 + gQ_{\rm IR}^2 Q_{\rm P} + hQ_{\rm P}^2 Q_{\rm IR} \\ & + iQ_{\rm IR} Q_{\rm P}^3 + jQ_{\rm P} Q_{\rm IR}^3 + mQ_{\rm IR}^2 Q_{\rm P}^2. \end{aligned} \quad (5)$$

TABLE III. The values of the coefficients of the polynomial determined from a fit to the energy surfaces of amplitudes of $A_1(29)$ and distortion modes for reversal of polarization (PR) as well as polarization and magnetization (PMR).

Coefficients	PR	PMR
a_3 (meV/amu$^{3/2}$ Å^{-3})	-5.24×10^{-3}	0
a_4 (meV/amu^2 Å^{-4})	9.11×10^{-2}	0.17
b_3 (meV/amu$^{3/2}$ Å^{-3})	−24.61	−0.04
b_4 (meV/amu^2 Å^{-4})	25.33	70.01
g (meV/amu$^{3/2}$ Å^{-3})	0.25	3.71×10^{-3}
h (meV/amu$^{3/2}$ Å^{-3})	0.02	-1.15×10^{-4}
i (meV/amu^2 Å^{-4})	0.14	0.12
j (meV/amu^2 Å^{-4})	−4.67	−5.71
m (meV/amu^2 Å^{-4})	0.45	−0.78

Here, $Q_{\rm P}$ and $Q_{\rm IR}$ are the amplitudes of the distortion and $A_1(29)$ modes, respectively. The obtained coefficients are listed in Table III. For the PR case [Fig. 5(a)], it is worth noting that the energy surface of the IR mode becomes asymmetric due to the presence of odd-order terms of $Q_{\rm IR}$. Since the $A_1(29)$ mode does not exhibit any crystal symmetry breaking, the atomic displacements result from the excitation of the mode with both positive and negative amplitudes not being related by symmetry, resulting in the terms with an odd order of $Q_{\rm IR}$. More obvious asymmetry for PR than PMR is due to the presence of a larger $b_3 Q_{\rm IR}^3$ term. Significantly, both positive and negative values of $Q_{\rm IR}$ displace the minimum of the $Q_{\rm P}$ toward the negative direction. A positive $Q_{\rm IR}$ displacement shifts the potential minimum position to the negative $Q_{\rm P}$ direction by a modest amount, while the negative value of $Q_{\rm IR}$ generates an energy minimum at a significant negative value of the $Q_{\rm P}$ coordinate. Meanwhile, the magnitude of $Q_{\rm IR}$ affects the magnitude of the energy minimum shift. Larger $Q_{\rm IR}$ values imply a more significant energy shift. These behaviors can be attributed to the coupling constant j of the term $Q_{\rm IR}^3 Q_{\rm P}$ having the most considerable magnitude, and its sign determines whether the minimum occurs at positive or negative distortion mode amplitude. As a result, a state with reversed polarization is lower in energy and energetically favored. In the PMR case [Fig. 5(c)], the energy surface is antisymmetric with positive and negative amplitudes of the $A_1(29)$ mode, corresponding to a large $b_4 Q_{\rm IR}^4$. For a positive (negative) amplitude of $Q_{\rm IR}$, the original energy minimum is destabilized, and $Q_{\rm P}$ is moved to the negative (positive) direction due to the negative signs of the $Q_{\rm IR}^2 Q_{\rm P}^2$ and the $Q_{\rm IR}^3 Q_{\rm P}$.

From the above energy expression, the equation of motion can be obtained as follows, from which we can calculate the corresponding time evolutions of both IR and distortion modes following the Sec. II D, with a periodic midinfrared laser pulse $F(t)$ imposed on the system and resonant with the IR mode:

$$\begin{aligned} \ddot{Q}_{\rm IR} + \gamma_{\rm IR}\dot{Q}_{\rm IR} + \omega_{\rm IR}^2 Q_{\rm IR} = {} & -b_3 Q_{\rm IR}^2 - b_4 Q_{\rm IR}^3 - 2gQ_{\rm IR}Q_{\rm P} - hQ_{\rm P}^2 \\ & - iQ_{\rm P}^3 - 3jQ_{\rm P}Q_{\rm IR}^2 - 2mQ_{\rm IR}Q_{\rm P}^2 + F(t) \\ \ddot{Q}_{\rm P} + \gamma_{\rm P}\dot{Q}_{\rm P} - \tfrac{1}{2}\omega_{\rm P}^2 Q_{\rm P} = {} & -a_3 Q_{\rm P}^2 - a_4 Q_{\rm P}^3 - gQ_{\rm IR}^2 - 2hQ_{\rm IR}Q_{\rm P} \\ & - 3iQ_{\rm P}^2 Q_{\rm IR} - jQ_{\rm IR}^3 - 2mQ_{\rm P}Q_{\rm IR}^2, \end{aligned} \quad (6)$$

where γ_{IR} and γ_P are the damping constants of the IR and distortion modes, respectively [63]. The function $F(t) = F\sin(\omega t)e^{-t^2/(2\tau^2)}$ is the driving pulse with amplitude F, frequency ω, and τ as the full width at a half-maximum duration of a pulse. The pulse shape has a symmetric Gaussian profile with a constant pulse duration of $\tau = 250$ fs and a pump frequency of $\omega = 1.03\,\omega_{IR}$ as used in previous midinfrared excitation simulations [14]. The resulting evolutions of the amplitudes of the IR (red line) and distortion (blue line) modes for both cases are shown in Figs. 5(b) and 5(d).

The responses of Q_{IR} in two instances display similar trends to the external excitation, which shows an oscillation with time, as well as Q_P. In the absence of pulse and nonlinear coupling interactions, the initial position of the Q_P oscillation is around its original equilibrium position, corresponds to the initial state. In the beginning, the IR mode is pumped by $F(t)$ and is forced to oscillate periodically about its equilibrium position. Upon excitation of the IR mode, the nonlinear coupling increases Q_P toward higher values, and the ferroelectric polarization and magnetization retain at all times the same sign of the initial state. With the time evolutions, the Q_P drops off rapidly, and its sign reorients from the original positive arrangement to the negative direction for a pump amplitude, corresponding to the reversal of the polarization [Fig. 5(b)] and magnetization [Fig. 5(d)] with the pulse amplitude reaching 9900 and 21 600 $\text{Å}\sqrt{\text{amu}}/\text{ps}^2$, respectively. The stronger external excitation needed for the magnetization reversal than for polarization reversal is consistent with the situation in which the energy barrier along the transition path is higher for magnetization switching than polarization switching. The maximum amplitude of the IR mode induced by magnetization reversal is higher than the amplitude caused by polarization switching, consistent with a larger pulse amplitude and strength. Note that the strength of the external pulse can be further reduced by decreasing the transition barrier in the situation of the epitaxial thin films or other types of design of fabricated structures [15,17,31,41]. The actual experimental switching path will be more complex, and polarization and magnetization switching under an applied electric field is thought to occur via a two-step switching process [58] or domain-wall motion [54,64]. In conclusion, selective excitation of the IR mode using a midinfrared pulse can switch the ferroelectric polarization and magnetization directions of BFO on an ultrafast timescale of several picoseconds.

IV. CONCLUSION

In summary, we found a strong coupling between the $A_1(29)$ IR phonon branch and the FE/AFD distortion modes, and we highlighted a method of frequency-controlled ultrafast selective switching of ferroelectric polarization or magnetization in BFO, using first-principles calculations. Using our processes, we predicted their dynamics when the IR branch was externally pumped by midinfrared laser pulses and we found that the switching of polarization or magnetization can occur at around 1 ps. Furthermore, the external excitation needed for the magnetization reversal is stronger than that of polarization reversal, which can be attributed mainly to the difference in transition barriers.

The approach presented here is a simple method for evaluating the possibility of ultrafast switching control of order states by a midinfrared THz laser pulse. It is generally applicable to a complex structural transition to further motivate the exploration of the midinfrared pulse as an effective method for manipulating functional material properties on ultrafast timescales, and it is promising to accelerate memory materials discovery.

ACKNOWLEDGMENTS

This work was supported by the National Natural Science Foundation of China (Grants No. 51790494, No. 12088101, No. 52072209, No. 51972033, and No. 61774020), Fundamental Research Funds for the Central Universities (Grant No. 2021XD-A06-1), Science and Technology Plan of Shenzhen City (Grants No. JCYJ20180306173235924 and No. JCYJ20180305164708625).

[1] E. Dagotto, Complexity in strongly correlated electronic systems, Science **309**, 257 (2005).

[2] P. Ravindran, R. Vidya, A. Kjekshus, H. Fjellvåg, and O. Eriksson, Theoretical investigation of magnetoelectric behavior in $BiFeO_3$, Phys. Rev. B **74**, 224412 (2006).

[3] J. Íñiguez, M. Stengel, S. Prosandeev, and L. Bellaiche, First-principles study of the multimode antiferroelectric transition in $PbZrO_3$, Phys. Rev. B **90**, 220103(R) (2014).

[4] U. V. Waghmare and K. M. Rabe, *Ab initio* statistical mechanics of the ferroelectric phase transition in $PbTiO_3$, Phys. Rev. B **55**, 6161 (1997).

[5] V. A. Abalmasov, Ultrafast reversal of the ferroelectric polarization by a midinfrared pulse, Phys. Rev. B **101**, 014102 (2020).

[6] J. Li, B. Nagaraj, H. Liang, W. Cao, C. H. Lee, and R. Ramesh, Ultrafast polarization switching in thin-film ferroelectrics, Appl. Phys. Lett. **84**, 1174 (2004).

[7] A. V. Kimel, A. M. Kalashnikova, A. Pogrebna, and A. K. Zvezdin, Fundamentals and perspectives of ultrafast photoferroic recording, Phys. Rep. **852**, 1 (2020).

[8] A. Kirilyuk, A. V. Kimel, and T. Rasing, Laser-induced magnetization dynamics and reversal in ferrimagnetic alloys, Rep. Prog. Phys. **76**, 026501 (2013).

[9] X. Li, T. Qiu, J. Zhang, E. Baldini, J. Lu, A. M. Rappe, and K. A. Nelson, Terahertz field-induced ferroelectricity in quantum paraelectric $SrTiO_3$, Science **364**, 1079 (2019).

[10] D. M. Juraschek and N. A. Spaldin, Sounding out optical phonons, Science **357**, 873 (2017).

[11] D. M. Juraschek and S. F. Maehrlein, Sum-frequency ionic raman scattering, Phys. Rev. B **97**, 174302 (2018).

[12] D. M. Juraschek, T. Neuman, and P. Narang, Giant phonon-induced effective magnetic fields in 4f paramagnets, arXiv:2007.10556.

[13] A. Subedi, Light-control of materials via nonlinear phononics, C. R. Phys. **22**, 161 (2021).

[14] A. Subedi, Proposal for ultrafast switching of ferroelectrics using midinfrared pulses, Phys. Rev. B **92**, 214303 (2015).

[15] R. Mankowsky, A. von Hoegen, M. Först, and A. Cavalleri, Ultrafast Reversal of the Ferroelectric Polarization, Phys. Rev. Lett. **118**, 197601 (2017).

[16] A. Subedi, Midinfrared-light-induced ferroelectricity in oxide paraelectrics via nonlinear phononics, Phys. Rev. B **95**, 134113 (2017).

[17] T. F. Nova, A. S. Disa, M. Fechner, and A. Cavalleri, Metastable ferroelectricity in optically strained $SrTiO_3$, Science **364**, 1075 (2019).

[18] R. Mankowsky, A. Subedi, M. Först, S. O. Mariager, M. Chollet, H. T. Lemke, J. S. Robinson, J. M. Glownia, M. P. Minitti, A. Frano, M. Fechner, N. A. Spaldin, T. Loew, B. Keimer, A. Georges, and A. Cavalleri, Nonlinear lattice dynamics as a basis for enhanced superconductivity in $YBa_2Cu_3O_{6.5}$, Nature (London) **516**, 71 (2014).

[19] M. Fechner and N. A. Spaldin, Effects of intense optical phonon pumping on the structure and electronic properties of yttrium barium copper oxide, Phys. Rev. B **94**, 134307 (2016).

[20] A. Subedi, A. Cavalleri, and A. Georges, Theory of nonlinear phononics for coherent light control of solids, Phys. Rev. B **89**, 220301(R) (2014).

[21] M. Rini, R. Tobey, N. Dean, J. Itatani, Y. Tomioka, Y. Tokura, R. W. Schoenlein, and A. Cavalleri, Control of the electronic phase of a manganite by mode-selective vibrational excitation, Nature (London) **449**, 72 (2007).

[22] V. Esposito, M. Fechner, R. Mankowsky, H. Lemke, M. Chollet, J. M. Glownia, M. Nakamura, M. Kawasaki, Y. Tokura, U. Staub, P. Beaud, and M. Först, Nonlinear Electron-Phonon Coupling in Doped Manganites, Phys. Rev. Lett. **118**, 247601 (2017).

[23] A. D. Caviglia, R. Scherwitzl, P. Popovich, W. Hu, H. Bromberger, R. Singla, M. Mitrano, M. C. Hoffmann, S. Kaiser, P. Zubko, S. Gariglio, J. M. Triscone, M. Först, and A. Cavalleri, Ultrafast Strain Engineering in Complex Oxide Heterostructures, Phys. Rev. Lett. **108**, 136801 (2012).

[24] R. I. Tobey, D. Prabhakaran, A. T. Boothroyd, and A. Cavalleri, Ultrafast Electronic Phase Transition in $La_{1/2}Sr_{3/2}Mn\,O_4$ by Coherent Vibrational Excitation: Evidence for Nonthermal Melting of Orbital Order, Phys. Rev. Lett. **101**, 197404 (2008).

[25] M. Först, R. I. Tobey, S. Wall, H. Bromberger, V. Khanna, A. L. Cavalieri, Y. -D. Chuang, W. S. Lee, R. Moore, W. F. Schlotter, J. J. Turner, O. Krupin, M. Trigo, H. Zheng, J. F. Mitchell, S. S. Dhesi, J. P. Hill, and A. Cavalleri, Driving magnetic order in a manganite by ultrafast lattice excitation, Phys. Rev. B **84**, 241104(R) (2011).

[26] M. Först, A. D. Caviglia, R. Scherwitzl, R. Mankowsky, P. Zubko, V. Khanna, H. Bromberger, S. B. Wilkins, Y. D. Chuang, W. S. Lee, W. F. Schlotter, J. J. Turner, G. L. Dakovski, M. P. Minitti, J. Robinson, S. R. Clark, D. Jaksch, J. M. Triscone, J. P. Hill, S. S. Dhesi, and A. Cavalleri, Spatially resolved ultrafast magnetic dynamics initiated at a complex oxide heterointerface, Nat. Mater. **14**, 883 (2015).

[27] M. Fechner, A. Sukhov, L. Chotorlishvili, C. Kenel, J. Berakdar, and N. A. Spaldin, Magnetophononics: Ultrafast spin control through the lattice, Phys. Rev. Mater. **2**, 064401 (2018).

[28] T. F. Nova, A. Cartella, A. Cantaluppi, M. Först, D. Bossini, R. V. Mikhaylovskiy, A. V. Kimel, R. Merlin, and A. Cavalleri, An effective magnetic field from optically driven phonons, Nat. Phys. **13**, 132 (2017).

[29] D. M. Juraschek, M. Fechner, and N. A. Spaldin, Ultrafast Structure Switching through Nonlinear Phononics, Phys. Rev. Lett. **118**, 054101 (2017).

[30] D. Afanasiev, J. R. Hortensius, B. A. Ivanov, A. Sasani, E. Bousquet, Y. M. Blanter, R. V. Mikhaylovskiy, A. V. Kimel, and A. D. Caviglia, Ultrafast control of magnetic interactions via light-driven phonons, Nat. Mater. **20**, 607 (2021).

[31] M. Q. Gu and J. M. Rondinelli, Nonlinear phononic control and emergent magnetism in Mott insulating titanates, Phys. Rev. B **98**, 024102 (2018).

[32] B. F. Grosso and N. A. Spaldin, Prediction of low-energy phases of $BiFeO_3$ with large unit cells and complex tilts beyond glazer notation, Phys. Rev. Mater. **5**, 054403 (2021).

[33] Y. Song, B. Xu, and C. W. Nan, Lattice and spin dynamics in multiferroic $BiFeO_3$ and $RMnO_3$, Natl. Sci. Rev. **6**, 642 (2019).

[34] J. Buhot, C. Toulouse, Y. Gallais, A. Sacuto, R. de Sousa, D. Wang, L. Bellaiche, M. Bibes, A. Barthélémy, A. Forget, D. Colson, M. Cazayous, and M-A. Measson, Driving Spin Excitations by Hydrostatic Pressure in $BiFeO_3$, Phys. Rev. Lett. **115**, 267204 (2015).

[35] P. Khan, M. Kanamaru, K. Matsumoto, T. Ito, and T. Satoh, Ultrafast light-driven simultaneous excitation of coherent terahertz magnons and phonons in multiferroic $BiFeO_3$, Phys. Rev. B **101**, 134413 (2020).

[36] S. Bhattacharjee, D. Rahmedov, D. Wang, J. Íñiguez, and L. Bellaiche, Ultrafast Switching of the Electric Polarization and Magnetic Chirality in $BiFeO_3$ by an Electric Field, Phys. Rev. Lett. **112**, 147601 (2014).

[37] D. S. Rana, I. Kawayama, K. Mavani, K. Takahashi, H. Murakami, and M. Tonouchi, Understanding the nature of ultrafast polarization dynamics of ferroelectric memory in the multiferroic $BiFeO_3$, Adv. Mater. **21**, 2881 (2009).

[38] M. Lejman, G. Vaudel, I. C. Infante, P. Gemeiner, V. E. Gusev, B. Dkhil, and P. Ruello, Giant ultrafast photo-induced shear strain in ferroelectric $BiFeO_3$, Nat. Commun. **5**, 4301 (2014).

[39] C. Paillard, B. Xu, B. Dkhil, G. Geneste, and L. Bellaiche, Photostriction in Ferroelectrics from Density Functional Theory, Phys. Rev. Lett. **116**, 247401 (2016).

[40] M. M. Yang and M. Alexe, Light-induced reversible control of ferroelectric polarization in $BiFeO_3$, Adv. Mater. **30**, 1704908 (2018).

[41] Y. D. Liou, S. Z. Ho, W. Y. Tzeng, Y. C. Liu, P. C. Wu, J. D. Zheng, R. Huang, C. G. Duan, C. Y. Kuo, C. W. Luo, Y. C. Chen, and J. C. Yang, Extremely fast optical and nonvolatile control of mixed-phase multiferroic $BiFeO_3$ via instantaneous strain perturbation, Adv. Mater. **33**, 2007264 (2021).

[42] Y. D. Liou, Y. Y. Chiu, R. T. Hart, C. Y. Kuo, Y. L. Huang, Y. C. Wu, R. V. Chopdekar, H. J. Liu, A. Tanaka, C. T. Chen, C. F. Chang, L. H. Tjeng, Y. Cao, V. Nagarajan, Y. H. Chu, Y. C. Chen, and J. C. Yang, Deterministic optical control of room temperature multiferrocity in $BiFeO_3$ thin films, Nat. Mater. **18**, 580 (2019).

[43] G. Henkelman, B. P. Uberuaga, and H. Jónsson, A climbing image nudged elastic band method for finding saddle points and minimum energy paths, J. Chem. Phys. **113**, 9901 (2000).

[44] B. J. Campbell, H. T. Stokes, D. E. Tanner, and D. M. Hatch, ISODISPLACE: A web-based tool for exploring structural distortions, J. Appl. Crystallogr. **39**, 607 (2006).

[45] R. Samnakay, D. Wickramaratne, T. R. Pope, R. K. Lake, T. T. Salguero, and A. A. Balandin, Zone-folded phonons and the commensurate-incommensurate charge-density-wave transition in 1T-$TaSe_2$ thin films, Nano Lett. **15**, 2965 (2015).

[46] A. Togo and I. Tanaka, First principles phonon calculations in materials science, Scr. Mater. **108**, 1 (2015).

[47] W. Li, J. Carrete, N. A. A. Katcho, and N. Mingo, ShengBTE: A solver of the Boltzmann transport equation for phonons, Comput. Phys. Commun. **185**, 1747 (2014).

[48] A. Togo, L. Chaput, and I. Tanaka, Distributions of phonon lifetimes in brillouin zones, Phys. Rev. B **91**, 094306 (2015).

[49] G. Kresse and J. Furthmüller, Efficiency of ab-initio total energy calculations for metals and semiconductors using a plane-wave basis set, Comput. Mater. Sci. **6**, 15 (1996).

[50] G. Kresse and D. Joubert, From ultrasoft pseudopotentials to the projector augmented-wave method, Phys. Rev. B **59**, 1758 (1999).

[51] P. E. Blöchl, Projector augmented-wave method, Phys. Rev. B **50**, 17953 (1994).

[52] J. P. Perdew, K. Burke, and M. Ernzerhof, Generalized Gradient Approximation Made Simple, Phys. Rev. Lett. **77**, 3865 (1996).

[53] R. D. King-Smith and D. Vanderbilt, Theory of polarization of crystalline solids, Phys. Rev. B **47**, 1651 (1993).

[54] J. B. Neaton, C. Ederer, U. V. Waghmare, N. A. Spaldin, and K. M. Rabe, First-principles study of spontaneous polarization in multiferroic $BiFeO_3$, Phys. Rev. B **71**, 014113 (2005).

[55] S. Steiner, S. Khmelevskyi, M. Marsmann, and G. Kresse, Calculation of the magnetic anisotropy with projected-augmented-wave methodology and the case study of disordered $Fe_{1-x}Co_x$ alloys, Phys. Rev. B **93**, 224425 (2016).

[56] C. Ederer and N. A. Spaldin, Weak ferromagnetism and magnetoelectric coupling in bismuth ferrite, Phys. Rev. B **71**, 060401(R) (2005).

[57] J. T. Zhang, X. M. Lu, J. Zhou, H. Sun, J. Su, C. C. Ju, F. Z. Huang, and J. S. Zhu, Origin of magnetic anisotropy and spiral spin order in multiferroic $BiFeO_3$, Appl. Phys. Lett. **100**, 242413 (2012).

[58] J. T. Heron, J. L. Bosse, Q. He, Y. Gao, M. Trassin, L. Ye, J. D. Clarkson, C. Wang, J. Liu, S. Salahuddin, D. C. Ralph, D. G. Schlom, J. Íñiguez, B. D. Huey, and R. Ramesh, Deterministic Switching of Ferromagnetism at Room Temperature Using an Electric Field, Nature (London) **516**, 370 (2014).

[59] J. M. Munro, H. Akamatsu, H. Padmanabhan, V. S. Liu, Y. Shi, L. Q. Chen, B. K. VanLeeuwen, I. Dabo, and V. Gopalan, Discovering minimum energy pathways via distortion symmetry groups, Phys. Rev. B **98**, 085107 (2018).

[60] P. Hermet, M. Goffinet, J. Kreisel, and Ph. Ghosez, Raman and infrared spectra of multiferroic bismuth ferrite from first principles, Phys. Rev. B **75**, 220102(R) (2007).

[61] M. Veithen, X. Gonze, and Ph. Ghosez, First-Principles Study of the Electro-Optic Effect in Ferroelectric Oxides, Phys. Rev. Lett. **93**, 187401 (2004).

[62] R. Mankowsky, M. Först, T. Loew, J. Porras, B. Keimer, and A. Cavalleri, Coherent modulation of the $YBa_2Cu_3O_{6+x}$ atomic structure by displacive stimulated ionic Raman scattering, Phys. Rev. B **91**, 094308 (2015).

[63] B. K. Das, B. Ramachandran, A. Dixit, M. S. Ramachandra Rao, R. Naik, A. T. Sathyanarayana, T. N. Sairam, and G. Amarendra, Emergence of two-magnon modes below spin-reorientation transition and phonon-magnon coupling in bulk $BiFeO_3$: An infrared spectroscopic study, J. Alloys Compd. **832**, 154754 (2020).

[64] A. Tagantsev, I. Stolichnov, E. Colla, and N. Setter, Polarization fatigue in ferroelectric films: Basic experimental findings, phenomenological scenarios, and microscopic features, J. Appl. Phys. **90**, 1387 (2001).